SCIENTIFIC REPORTS

OPEN

SUBJECT AREAS:
CRYOSPHERIC SCIENCE
CLIMATE CHANGE
ATTRIBUTION
PROJECTION AND PREDICTION

Received
11 April 2013

Accepted
1 July 2013

Published
24 July 2013

Correspondence and requests for materials should be addressed to J.S.L. (joe.levy@utexas.edu)

Accelerated thermokarst formation in the McMurdo Dry Valleys, Antarctica

Joseph S. Levy[1], Andrew G. Fountain[2], James L. Dickson[3], James W. Head[3], Marianne Okal[4], David R. Marchant[5] & Jaclyn Watters[1]

[1]University of Texas Institute for Geophysics, Jackson School of Geosciences, University of Texas at Austin, Austin, TX, USA, [2]Department of Geology, Portland State University, Portland, OR, 97210, [3]Department of Geological Sciences, Brown University, Providence, RI, 02912, [4]UNAVCO, Boulder, CO 80301, [5]Department of Earth & Environment, Boston University, Boston, MA, 02215.

Thermokarst is a land surface lowered and disrupted by melting ground ice. Thermokarst is a major driver of landscape change in the Arctic, but has been considered to be a minor process in Antarctica. Here, we use ground-based and airborne LiDAR coupled with timelapse imaging and meteorological data to show that 1) thermokarst formation has accelerated in Garwood Valley, Antarctica; 2) the rate of thermokarst erosion is presently ~ 10 times the average Holocene rate; and 3) the increased rate of thermokarst formation is driven most strongly by increasing insolation and sediment/albedo feedbacks. This suggests that sediment enhancement of insolation-driven melting may act similarly to expected increases in Antarctic air temperature (presently occurring along the Antarctic Peninsula), and may serve as a leading indicator of imminent landscape change in Antarctica that will generate thermokarst landforms similar to those in Arctic periglacial terrains.

Although thermokarst landforms have been previously mapped in coastal Antarctica, including within the McMurdo Dry Valleys (MDV)[1–6], it has been uncertain whether these landforms are equilibrium landforms[7,8] gradually evolving at a constant rate[2,3,7,9], or whether thermokarst development is accelerating as a result of modern changes to thermal boundary conditions[1,8]. Garwood Valley (78°S, 164°E) is a coastal valley in the McMurdo Dry Valleys (MDV) of Southern Victoria Land, Antarctica and is a natural laboratory in which competing models of Antarctic thermokarst erosion can be tested. The valley lies in a zone of continuous permafrost (mean annual air temperature is −16.9°C) and is partially filled with a remnant of the Ross Sea Ice Sheet, a debris-covered ice mass that lodged in the valley during the Pleistocene[1,10] (Fig. 1). The remnant debris-covered ice extends ~ 7 km up-valley from the modern Ross Sea coast, draping surfaces ranging in elevation from sea-level to ~ 200 m a.s.l. The ablation till overlying the buried ice is typically ~ 10–20 cm thick, but thickens in places up to several meters[1,11]. The till has been subdivided into up-valley (older) and down-valley (younger) units, both of which are of Pleistocene age[1], and is composed largely of a sand-silt matrix overlain by a pebble, cobble, and boulder desert pavement[1,11]. In the center of the valley and at the ice cliff study site (see below), the buried remnant of the Ross Sea Ice Sheet is overlain by thin glacial till and is capped by fluvio-deltaic sediments deposited into the Pleistocene-to-Holocene aged paleolake, Lake Howard[1,9,12], a small, < 0.7 km^2 lake that formed within and atop the Ross Sea Ice Sheet ice dam[1]. Active layer thickness in Garwood Valley is typically ~ 20 cm, and the base of the active layer is typically marked by the sharp contact between buried ice and the overlying till[1,11]. The base of the active layer is typically wet (5–10% water by volume) in thin tills, and dry for thicker tills that are not in contact with the buried ice.

The buried ice mass in Garwood Valley is ablating[1], which produces a variety of thermokarst landforms, including thermokarst ponds[11,13–15], tunnels and/or thermokarst dolines eroded through buried ice by the modern Garwood River[9,16–20], and a large retrogressive thaw feature referred to as the Garwood Valley ice cliff[1,8] (Fig. 2). The Garwood River is sourced largely by glacial runoff from the Garwood and Joyce glaciers, and flows ~ 13 km down-valley from the toe of the Garwood Glacier to the Ross Sea coast. The river is < 50 cm at its deepest. The Garwood River incises the valley floor to a depth of ~ 4 m, and buried ice is commonly observable in the steep, v-shaped river channel walls[1–3,9].

The ice cliff is a location where 10–15 m of the remnant Ross Sea Ice Sheet ice is exposed at a precipitous break in slope adjacent to the modern Garwood River braid plain[1]. The Garwood River main channel meanders ~ 1–2 m over ~ 10 m wavelengths in the vicinity of the ice cliff, in places undercutting the exposed base of the cliff and

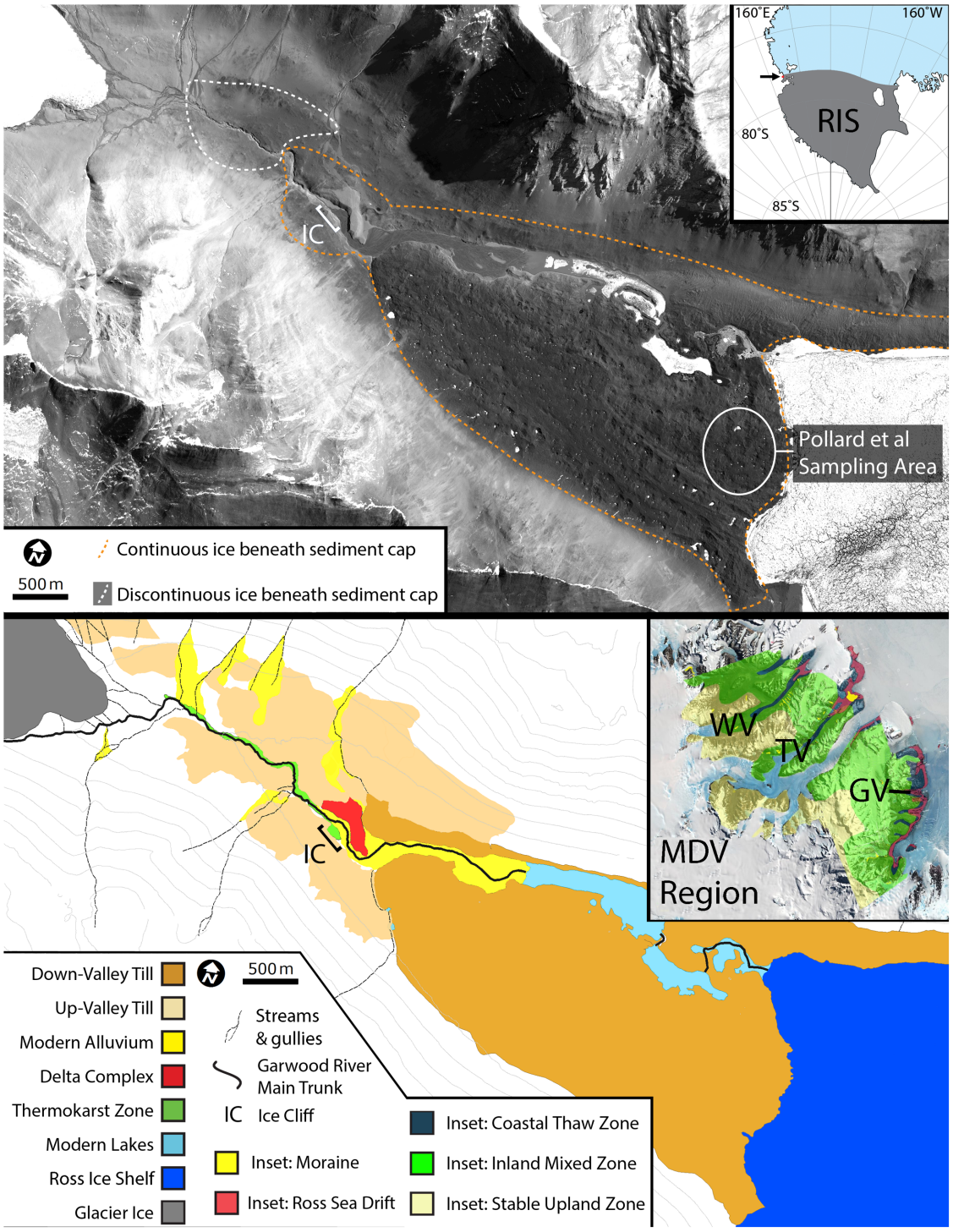

Figure 1 | (Above) Quickbird satellite image of Garwood Valley (image data courtesy the Polar Geospatial Data Center). Mapped ice extents are based on field observations of exposed ice and ground penetrating radar[34]. Contours are at 100 m intervals. Inset location map shows the Ross Sea region, the modern Ross Ice Shelf (RIS), the southern MDV (arrow), and the location of Garwood Valley (red dot). (Below) Geomorphic map of Garwood Valley surface units. Inset shows extent of ice-cored landscapes and buried ice in the McMurdo Dry Valleys (MDV). GV indicates location of Garwood Valley, TV of Taylor Valley, and WV of Wright Valley.

in others, flowing in a sandy channel several meters from the cliff. Since 2009, ablation of the ice cliff has moved the face of the cliff southwards, relative to the location of the river channel. During high flow, the Garwood River becomes braided and can fill additional small channels north of the main channel (away from the ice cliff) (see SI).

The ice exposed at the Garwood ice cliff is geochemically identical to the massive ice buried by the down-valley till (statistically indistinguishable major ions, $\delta^{18}O$ and δD values within the range of Ross Sea Ice Sheet variability), suggesting that ice exposed at the ice cliff and at other points down valley are composed of the same buried Ross Sea Ice Sheet material (Fig. 1)[1,12]. The ice cliff ice is capped by ~ 2 m of ice-cemented glacial till and fluvial sediments, of which the upper ~ 20 cm seasonally thaws. It has a generally north-facing aspect, but portions of the cliff face east and west as well.

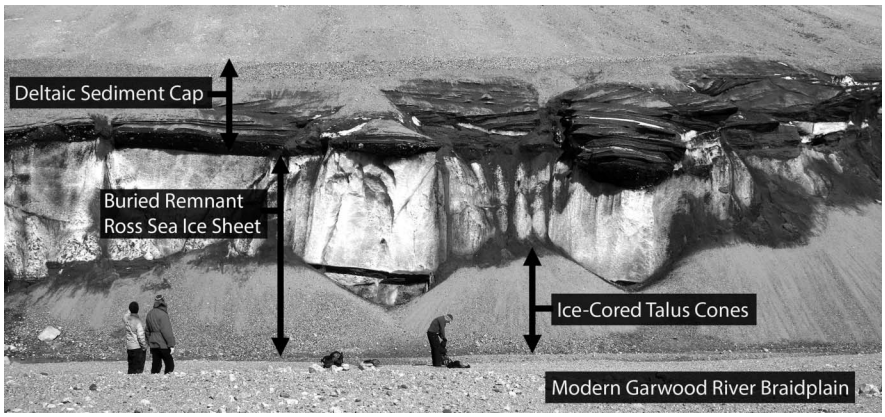

Figure 2 | The Garwood Valley ice cliff. Personnel are ~ 50 m in front of the cliff, which is 10–15 m tall. Image credit: Jim O'Connor.

Field observations of the Garwood Valley ice cliff indicate that it is backwasting rapidly (see time lapse video in Supplementary Information)[1,12]. In contrast, Pollard et al.[1,11] inferred that the buried ice located between the ice cliff and the mouth of Garwood Valley was in near-equilibrium with modern climate conditions because the thermokarst ponds are largely confined to the valley mouth—although they noted that small changes in ground temperature could lead to more widespread thermokarst formation in the valley.

Two primary hypotheses have been proposed to account for the formation of thermokarst landforms in the MDV: 1) small increases in summer air temperature result in small increases in active layer thickness that drive deeper melting[1,11] and 2) surface-to-subsurface flow of warm meltwater advects heat to buried ice[9,20–22]. Other geological heat sources are unlikely to contribute to ground ice melting in Garwood Valley: mapping[1] indicates that no active fault-directed hydrothermal features or volcanic features are present in the valley, and geothermal heat flux in the MDV is generally low (~ 50 mW/m^2)[23,24]. In order to test these thermokarst generation hypotheses and to suggest new ones to test, an observation system was established at the Garwood Valley ice cliff consisting of a continuous monitoring station ~ 8 m north of the ice cliff (Fig. 3–4) (see methods section), a time-lapse camera system (see SI), and biannual terrestrial laser scanning (ground-based LiDAR) of the ice cliff and vicinity (Fig. 5). The continuous monitoring station measures air temperature and relative humidity, ice cliff surface temperature via infrared radiometry, range to the ice cliff via ultrasonic distance sensor, wind speed and direction, and longwave and shortwave radiation balance. The radiation sensors are oriented such that they measure the fluxes into and out of the ice cliff, rather than the traditional incoming (upward-facing) and outgoing (downward-facing) directions. The continuous monitoring station is shadowed at night because the low sun angle places the sun behind the south valley wall from ~ 20:00 to 06:00 (see SI); the ice cliff and station are illuminated only by diffuse insolation during these hours.

Results

Biannual LiDAR scans show large-scale thermokarst backwasting occurring along the entire face of the ice cliff (Fig. 5). Since ground-based data collection began in November 2010 to January, 2012, the ~ 400 m long ice cliff has backwasted ~ 1–3 m. Since airborne LiDAR data were first collected in 2001–2002 to January, 2012, backwasting along the ice cliff has ranged from 10–55 m, totaling 44,900 ± 900 m^3, or on average, 5,000 ± 100 m^3/year. From November 2010 to January 2011, 6,700 ± 130 m^3 of ice and capping sediment was removed from the Garwood Valley ice cliff; from January 2011 to January 2012, 11,300 ± 230 m^3 of material was removed.

These measurements of ice cliff volume change are supported by continuous (15 minute interval) measurements of the distance between the ice cliff and the continuous monitoring station (Fig. 3). Continuous measurements show a gradual increase in range from 29 January 2011 to 22 February 2011 (104 cm total, ~ 4.3 cm/day average, austral summer 2010–2011), little change from then to 22 August 2011 (austral winter 2011), rapid fluctuations in range until 12 November 2011 (austral spring), and gradual, but accelerating increases in range totaling 95 cm (~ 2.0 cm/day) through 30 December, 2011 (austral summer 2011). These ice cliff retreat rates are comparable to the low range of recent measurements of erosion rates for coastal Arctic and Tibetan retrogressive thaw slumps (< 1 to 9 m/year, with extreme headwalls producing 30 m/year retreats)[20–22,25]. For comparison, measured ablation rates (melt and sublimation) of alpine glaciers and lake ice in the MDV span 20–44 cm/year[26–31]. Unlike the ice cliff, Quickbird satellite observations (60 cm/pixel) and field observations from 2009 to 2012 show little or no change in thermokarst pond shape or abundance in the downvalley till.

These continuous range measurements, coupled with time-lapse photography (see SI) indicate two modes of thermokarst activity at the Garwood Valley ice cliff. One mode, melting, results in gradual retreat of the ice cliff and transport of overlying sediments downslope via meltwater runoff. The second mode, calving, results in block failure of ice and ice-cemented sediments. Melt is the dominant mechanism of ice cliff retreat, removing ~ 100 cm/year from the entire face of the ice cliff (Fig. 3) versus ~ 50 cm/year in discrete locations due to calving events. Calving events are less common than daily melting pulses, but result in dramatic step-changes in ice cliff position (Fig. 3). Calving accounts for the abrupt decrease in range to the ice cliff in November, 2011, when multiple ice blocks fell into the line of sight of the range sensor (Fig. 4). Melting and/or continued downslope movement of the calved blocks out of the range sensor field of view is inferred to have resulted in a return to consistent ice cliff range values.

Using airborne LiDAR data collected in 2001[7,32], it is possible to determine whether the thermokarst backwasting at the Garwood Valley ice cliff is an extension of equilibrium conditions that have persisted throughout the Holocene, or are a departure from Holocene average conditions. Using 4 m/pixel airborne LiDAR data[7,16,33], the volume of the basin in which the ice cliff and the modern Garwood River braid plain are situated was determined to be 7,300,000 ± 150,000 m^3 (Fig. 5). This is the volume of sediment and ice that would have filled the topographically low area between the modern ice cliff and the paleo-lake deltas located north of the ice cliff, assuming that the two surfaces were connected by a flat continuum slope.

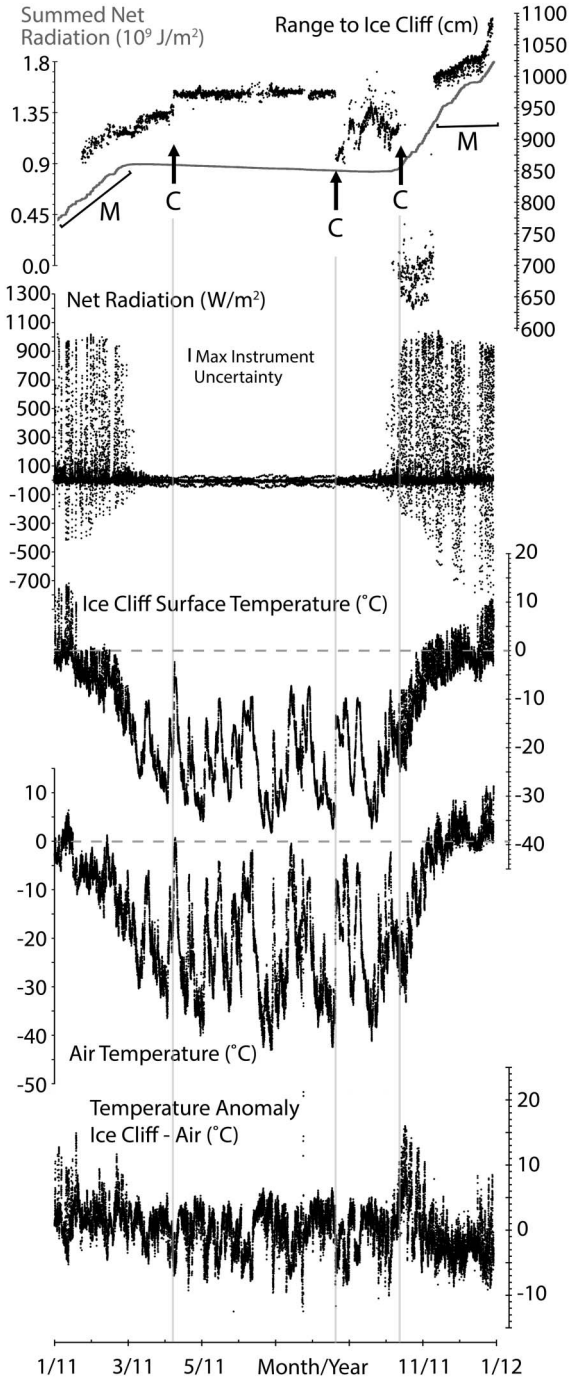

Figure 3 | Summary of continuous monitoring station data. Measurement uncertainties in range to ice cliff, air temperature, and ice cliff temperature are all smaller than marker size. Range, shortwave insolation, and temperature are recorded at 15-minute intervals. Summed net radiation integrates the net radiation (upwelling and downwelling longwave and shortwave) plot with respect to time, and reflects the total radiative energy balance of the ice cliff. Strongly negative energy balances during melting periods are inferred to result from specular reflection of longwave and shortwave radiation from the ice cliff during melting periods, which strongly increases radiation from the ice cliff[42]. M indicates regions of the range record when melting is inferred to have occurred. C represents an event interpreted to be due to calving. Vertical gray lines show the time of these events across plots. Temperature anomaly shows the difference between ice cliff temperature and air temperature (positive numbers indicate the ice cliff is warmer than the air). Air temperature data from 2011-8-24 05:15 to 2011-11-12 04:00 were extracted from an identical weather station located 4 km down-valley due to temperature data-drop-out at the ice cliff.

Figure 4 | The ice cliff and continuous monitoring station after a calving event. Tripod is 3 m tall. The Garwood River (frozen) can be seen to the right. Image taken 11 November, 2011. Photo credit: Thomas Nylen.

This assumption is reasonable because Garwood Valley supports a classic U-shaped transverse profile with no medial ridges or elevated topography in the valley centre. In addition, the deltaic sediments that overlie the ice cliff ablation till are stratigraphically and lithologically identical to the flat-lying, plane-bedding deltaic sediments located across the modern Garwood River from the ice cliff, suggesting that they were once part of a connected deltaic depositional surface[1,16,17]. The Garwood Valley paleo-lake deltas were deposited in a basin composed solely of buried Ross Sea Ice Sheet ice capped by $\sim$ 1 m of ablation till (the delta sediments overlie this till and buried ice at present)[1]. While some lateral erosion of the paleo-lake deltas has likely occurred due to erosion by the modern Garwood River, the presence of the paleo-lake deltas at the confluence between the ice-cored up-valley and down-valley till deposits (Fig. 1) strongly suggests that most of the material removed from between the paleo-lake deltas and the modern ice cliff was composed of buried ice capped by $\sim$ 1 m of ablation till and $\sim$ 1 m of deltaic sediments, similar to the stratigraphy of the ice cliff at present, suggesting that erosion rates and mechanisms for removing this material in the past were likely similar to those operating today.

The youngest deltaic sediments capping the ice cliff were emplaced within the last 6.3 ky, based on radiocarbon dating of an algal mat present in the sediments[1]. Because erosion of the ice cliff could not occur before the end of emplacement of deltaic sediments above the ice cliff (which were cut during incision of the ice cliff), this date provides a maximum age for the formation of the ice cliff. Accordingly, the average thermokarst erosion rate at the Garwood Valley ice cliff for the last 6.3 ky is 1150 $\pm$ 20 m^3/year (missing volume divided by time). Thus, the 2001–2010 average erosion rate ($\sim$ 5,400 m^3/yr) is $\sim$ 5 times the late-Holocene average, the 2010–2011 erosion rate (7,000 m^3/year) is $\sim$ 6 times the late-Holocene average, and the 2011–2012 erosion rate (11,400 m^3/year) is $\sim$ 10 times the late-Holocene average. These results show that thermokarst erosion at the ice cliff has accelerated.

Discussion

What physical processes dominate ice cliff melt, and how do these processes compare to prevailing models of thermokarst formation in the MDV and elsewhere? Air temperature has not been a primary driver of the observed ice cliff melt. Evidence for this is that the ice cliff continues to melt for more than one month after air temperatures at the base of the ice cliff drop below 0°C (Fig. 3). More generally, air temperature is not the driver of the accelerated melt rate along the ice cliff, because air (and soil) temperature in the MDV (recorded at the Lake Hoare meteorological station in Taylor Valley, $\sim$ 50 km north) has experienced a decadal cooling trend (−0.7°C/

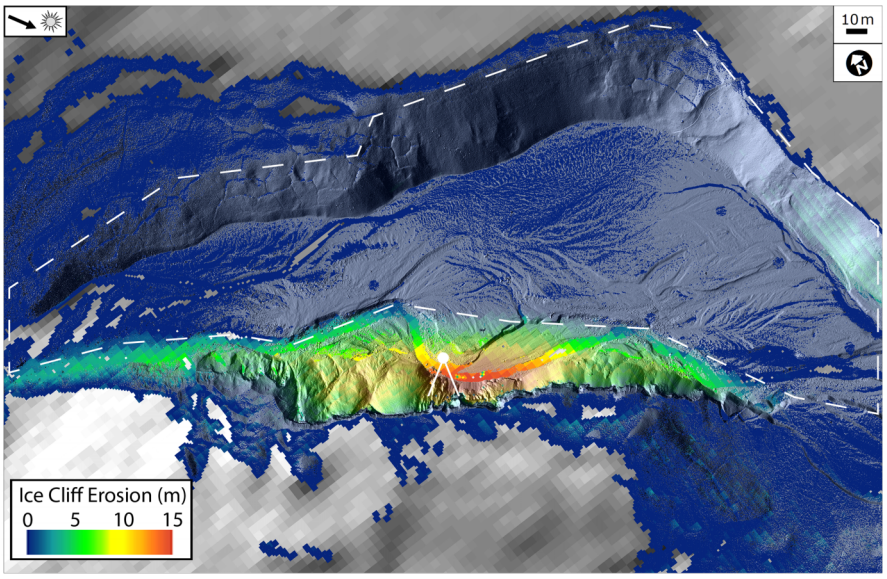

Figure 5 | Ice cliff thermokarst erosion (measured vertically from the 2001 surface—see SI) calculated by differencing the 2001 airborne LiDAR[7] and the January 2012 terrestrial laser scan. White dot indicates location of continuous measurement station. Solid white lines indicate infrared radiometer and sonic ranger field of view. Dashed line indicates area of erosion between initial ice/sediment deposition (Pleistocene/Holocene) and 2001. Base map is a hill-shade derived from the January 2012 TLS overlain on a hill-shade derived from 2001–2002 airborne LiDAR to extend the base map beyond the range of the ground-based scans. Arrow indicates illumination direction.

decade) spanning 1986–2000[23], which has largely leveled off over the past ~ 5 years (www.mcmlter.org, data downloaded April, 2013)—in stark contrast to warming along the Antarctic Peninsula (+0.4°C/decade)[25]. During the 2001–2012 span of LiDAR observations, neither mean annual air temperature, nor summer monthly average air temperature, nor summer peak daily air temperature have experienced statistically significant increases in the MDV (see SI). Although peak air temperatures enhance melting in particularly warm years, increasing air temperature does not seem to explain the acceleration of ice cliff thermokarst backwasting over decadal timescales.

If not air temperature increase[11], then are fluvial or aeolian processes the main generator of ice cliff thermokarst[9]? Major calving events shown in Figure 3 occurred during air temperature peaks associated with rapid increases of ice surface temperature of at least 10°C. In the first two cases, the increase is due to drainage wind events that are common during the winter in the MDV and which can increase air temperatures by more than 20°C in a few hours[26]. The third calving event shown in Figure 3 coincides with the initial illumination of the ice cliff after the end of winter darkness. This event is not associated with high winds. Accordingly, we hypothesize that these calving events result from the rapid thermal expansion of the ice during sudden warming events that destabilize ice blocks near the point of failure. Dry Valleys glaciers and frozen lakes commonly crack loudly during early and late season periods when the ice and air are both cold. These cracking periods coincide with abrupt changes in solar illumination. Finally, wind gusts, which can reach in excess of 30 m/s, may facilitate calving and slumping (see SI), but are not generally associated with rapid ice cliff retreat by melting or by ice-cemented sediment debris avalanching.

Is the Garwood River a major driver of thermal transfer or calving events at the ice cliff? The river undercuts the ice cliff, but there is commonly a gap of 1–10 cm between the water level and the base of the ice exposure (see SI). Accordingly, we infer that thermal transfer from river water to the ice is a secondary driver of ice cliff retreat (see SI). Undercutting by the Garwood River creates ice cliff overhangs, which are unstable, and that can result in mechanical failure of ice blocks, ice-cemented sediment, or dry sediment along the front of the ice cliff. These calving and slumping events can occur during sub-freezing conditions when the Garwood River is fully frozen (Fig. 4). Garwood River discharge is inferred to be at a millennial-scale low due to abundant snow cover on the Garwood and Joyce glaciers, which may represent cyclical reorganization of Southern Ocean and atmospheric circulation[32].

The physical factor most strongly correlated with ice cliff retreat by melting is total net radiation (Fig. 3), suggesting a new candidate melting mechanism to test in other ground-ice areas of the MDV[34]. Periods of positive net radiation balance are strongly associated with glacier melt in the MDV[27,32] and with ice cliff retreat in particular. Integrated net radiation closely tracks ice cliff range, even when air temperatures are below 0°C. Increased insolation provides an explanation for accelerating ice cliff retreat since 2001: since 1990, summer incoming solar radiation in the Dry Valleys has increased[34] ~ 35 W m^{-2} (~ 1.7 W/m^2/yr, $R^2 = 0.33$, $P < 0.01$). This is a large percentage of summer average insolation (~ 220 W/m^2 from 1990–2009) (See SI)[27], and represents a departure from the 1957–1994 continental trend of decreasing insolation in Antarctica[35].

Radiative control of ice cliff melting is supported by measurements of ice cliff surface temperature and by regional measurements of insolation. When air temperatures are below 0°C (e.g., February 2011), gradual melting occurs during periods of high net radiation, indicated by ice cliff surface temperatures that are pegged at or below 0°C (the temperature is fixed by melting—similar to behavior observed in active layer "zero curtain" conditions in which isothermal melting or freezing occurs in water-rich seasonally frozen soils). Net radiation at the ice cliff on sunny summer days is ~ 1.7–1.8 × 10^7 J/m^2, approximately double the latent heat required to maintain the melt rates at the ice cliff (2–4 cm/day) in the absence of sensible and turbulent heat fluxes from adjacent air.

Observations of ice cliff melting processes clearly show the direct deposition and meltwater-mediated transport of sediments overlying the ice cliff onto the ice cliff surface (Fig. 2 and SI). These low albedo sediments wash over the ice cliff and reduce its albedo from ~ 0.6 to 0.1, and are warmed during periods of intense insolation, providing a conductive source of sensible heat to the ice cliff, raising the apparent surface temperature of the ice cliff above 0°C, and dramatically

enhancing melting (e.g., during December 2011/January 2012) (see SI). Melting of ice-sediment mixtures is indicated in the continuous monitoring record by high ice temperature and by a reduction in shortwave albedo from typical values of 0.5 to low values of ~ 0.1 during melt periods (see SI). Increased insolation (1.7 $W/m^2/yr$) plus decreased ice albedo would be expected to generate several hundred cubic meters of additional ice melt per year along the ~ 400 m face of the ice cliff[16,33], assuming a 15 m tall ice cliff with uniform insolation distribution, latent heat of fusion of 334 kJ/kg ice, and a density of ice of 917 kg/m^3. Increased insolation of 1.7 $W/m^2/yr$ would produce an additional 260 m^3 of melt per year from baseline conditions, or an additional ~ 4 cm of melt back per year.

Are there feedbacks that would reduce ice cliff thermokarst melting? Ice-cored talus cones are a persistent landscape feature at the front of the ice cliff (Fig. 2). If melting of the ice cliff and transport of overlying sediments were burying the ice cliff in dry sediment, it might be cut off from insolation and buried to a depth deeper than the active layer (i.e., polycyclic behavior[20]). Burial of the ice cliff would appear in the LiDAR record as a decrease in slope along the ice cliff (from sheer ice cliff to low angle talus). Since 2010, the spatial distribution of slopes along the ice cliff has changed, however, the frequency of steep and shallow slopes has remained largely the same (see SI). Talus cones appear to migrate along the surface of the ice cliff, but are not presently burying it. The presence of the Garwood River at the base of the ice cliff removes the accumulated talus, preventing a protective cover from being established. The wall of the valley on the other side of the Garwood River shows little to no topographic change over the instrumental record (2010–2012) due to the talus cover over buried ice and a lack of evacuation by the river. It is possible that thicker debris covers in the past (e.g., during the mid-Holocene) inhibited ice cliff melt and erosion, but that enhanced melting during the study period has result in a transition to thinner debris covers and no inhibition of melting.

Could the accelerated formation of thermokarst in Garwood Valley, interpreted here to be driven by increasing insolation and sediment/ice interactions, provide a leading indicator of thermokarst formation that could disrupt the abundant ice-cored terrains[10] of the MDV? Increased insolation is already implicated in MDV lake-level rise driven by enhanced alpine glacier melt (see SI). Some ice-cored and ice-cemented landforms in Antarctica are thought to be vulnerable to disruption by future deepening of active layer thaw[6,11]. In addition to increases in shortwave radiation noted here, warming scenarios predict mean annual air temperatures in the MDV to rise between 1.6–3.5°C by 2100[13–15]. Elementary, conduction-based, active layer depth models[36] predict that even under mild warming conditions (e.g., 1–2°C), active layer depths in the MDV would increase 10–21 cm (for increases in mean annual ground temperature) and 4–8 cm if warming is confined purely to increases in peak summer temperatures, based on a mean thermal diffusivity for Garwood Valley sediments (0.27 mm^2/s, N = 6, standard deviation = 0.09). Such deepening of the active layer could generate widespread melting in the ice-cored regions of Garwood Valley, where the ice table is currently defined by the contact between buried ice and overlying sediments, and could act as a catalyst for the formation of additional retrogressive thaw features throughout Antarctic ice-rich terrain[16,17].

In summary, the Garwood Valley ice cliff, a thermokarst feature in coastal Antarctica, is losing volume at a rate approaching ten times its average late-Holocene ablation rate. The ablation rate for the ice cliff has increased in each of the three measurement windows: 2001–2010, November 2010 to January 2011, and January 2011 to January 2012. The current ablation rate exceeds the ablation rate for McMurdo Dry Valleys glaciers by a factor of five[28], and represents a major departure from typical land surface change rates in the Ross Sea sector of Antarctica. We interpret the main driver for current ice loss in Garwood Valley to be insolation-driven melting that results from increases in insolation coupled with an albedo-feedback in which overlying debris shed onto the ice cliff reduces the ice surface albedo and increases conductive heat transfer.

Future air and ground warming in the Dry Valleys may destabilize additional buried ice deposits[34], which when exposed at breaks in topography would be likely to experience a similar sediment/melting feedback to that observed at Garwood Valley. Such ice exposures would experience rapid ablation greater than that predicted by conductive thermal models alone[11], and may result in the generation of retrogressive thaw slumps and other thermokarst landforms that exhibit polycyclic periods of rapid melting in response to variations in ice exposure and sediment burial[13]. This process is not unique to the Dry Valleys, but is similar to ice/sediment interactions observed on non-polar debris-covered glaciers in which a thick mantle of debris insulates subsurface ice, allowing rapid melt to occur at bare ice locations where sensible heat and solar radiation can drive melting[37]. Garwood Valley ice cliff recession may be a leading indicator of more widespread landscape change that is expected to transform low elevation and coastal Antarctic landscapes by the close of the century. The acceleration of Antarctic thermokarst formation by future climate warming[13–15] may bring about the formation of degraded permafrost landforms in Antarctica similar to those generated in Arctic cold desert permafrost environments[16–20].

Methods

We collected terrestrial laser scanner (ground-based LiDAR) data used in this project using a Riegl VZ-400 in 2010–2012. The workflow for collecting data and producing a georeferenced point cloud is as follows. 1. Identify field site and plan survey in collaboration with UNAVCO. 2. Set up reference points. In this study, four permanent markers (pieces of rebar pounded into the permafrost) were installed in Garwood Valley ~ 100 m distant from the melting edge of the ice cliff. Tripods with reflective targets were then set up over these markers, leveling and centering the targets over the markers. Two additional reflective targets were set up at the study site to provide additional reference points for the survey. The targets were red, flat disks with a diameter between 10 cm and 12 cm. 3. Carry out the survey. An overall minimum point spacing of 5 cm across the specific areas of interest (AOIs) was achieved, and in some areas the point spacing is closer to 2 cm. The site was scanned from 4–7 scan positions, depending on time constraints, weather conditions, etc. While the scanning occurred, GPS coordinates for each one of the targets were collected using Trimble 5700s, which are differential grade GPS instruments. 4. Process the data.

For all scans, Riegl's proprietary software, RiSCAN Pro, was used to process the data. For each visit to the site, scans from each scan position were registered to each other. The whole site was then registered to the GPS data. Each LiDAR survey was conducted by collecting individual scans from different vantage points, called scan positions. The scans from each scan position were then registered or aligned to each other by using reflective targets that had been placed at the site for the duration of each LiDAR survey and consequently scanned as reference points which the scanner software, Riegl's RiSCAN Pro, is designed to recognize as such. When registering scans, RiSCAN Pro applies a proprietary algorithm to solve for the best fit; the standard deviation for each scan position's registration to the other scan positions is reported by the software and generally ranged from 0.005 m to 0.030 m. Once all of the scans for each individual survey are registered to each other, the complete scan is then georeferenced by applying GPS coordinates to the aforementioned reflective targets, or reference points. The GPS coordinates are obtained by placing differential-grade GPS receivers atop the reflective targets and solving to a nearby (< 10 km) local base station operating on a known benchmark. This typically results in a GPS solution with 1–3 cm accuracy in the horizontal and 2–5 cm accuracy in the vertical. The registration of the scan to the GPS reference points is again performed within RiSCAN Pro, and the process yields results typically with standard deviations of 1–5 cm. Registered and georeferenced point clouds from individual surveys can from this point onward be viewed and analyzed in the same coordinate system. LiDAR point clouds were output from RiSCAN Pro to XYZ ASCII files (latitude, longitude, elevation), which were then input into ArcMap as point shapefiles.

Point clouds were converted to 2.5D elevation rasters using the ArcMap point to raster conversion tool that produces a digital elevation model derived from draping a surface over the point cloud. Elevation raster pixels were set as the maximum point elevation in each 10 cm by 10 cm raster pixel. Where shadows existed in the LiDAR scans, values of NoData were assigned to the initial raster. In order find the differences between scans, NoData values were removed by conducting an interpolation between raster cells with data, using the average value of a moving 3 × 3 grid of cells around the NoData cell. Because the moving window for the interpolation ignores NoData values, it can provide an interpolation based on at least one data point for data gaps up to 40 cm long by 40 cm tall. Any data gaps larger than this are left as NoData values in the raster, are not used in subsequent data processing, rendering the volume change calculations minimum volume change values. In order to determine the difference between the 2001 airborne LiDAR and the TLS scans, the 2001 airborne LiDAR was

resampled to 1 m/pixel using bilinear interpolation and differenced from the TLS scans using the DEM differencing methodology outlined by[38,39]. Large (> 0.5 m) boulders that remained in fixed position between the scan periods provide an estimate of DEM accuracy, and are typically within ± 5 cm of each other between scans, indicating that the total DEM uncertainty derived from projection and interpolation of data[40] is smaller than the uncertainty produced by the coarsest point cloud uncertainty (± 5 cm, which, for this eroded volume produces a maximum volumetric uncertainty of ± 2%). Accordingly, LiDAR scans measure thermokarst erosion in terms of the displaced volume[41] of ice melted and sediment transported per year. In map view (e.g., Fig. 5), this is presented as vertical meters of ice/sediment removed in each horizontal pixel.

Continuous monitoring station measurements were collected using sensors connected to a Campbell Scientific CR10X datalogger. Instruments are installed on a cross arm at 3 m elevation. Incident and reflected shortwave radiation was measured using two Eppley precision spectral pyranometers (instrument intrinsic maximum measurement uncertainty of ± 3%). Incident and emitted longwave radiation was measured using two Eppley precision infrared radiometers (instrument intrinsic maximum measurement uncertainty of ± 5%). Ice cliff surface temperature was measured using an Apogee Instruments SI-111 infrared radiometer (instrument intrinsic maximum measurement uncertainty of ± 0.2°C with emissivity variability generating < 2% error). Range to the ice cliff was measured using a Scott Technical Instruments SR-50A ultrasonic distance sensor (instrument intrinsic maximum measurement uncertainty ± 4.4 cm, however, signal noise can rise to 25–50 cm during high wind events and/or when calving blocks and debris avalanches enter the sensor field of view). Air temperature and relative humidity at the continuous monitoring station at 3 m elevation were measured using a Vaisala HMP60 probe (instrument intrinsic maximum measurement uncertainty of ± 5%). Ground temperature in the sediments beneath the continuous monitoring station was measured using a Campbell Scientific 107 thermistor placed 1–2 cm below the ground surface (instrument intrinsic maximum measurement uncertainty of ± 0.5°C). Wind speed and direction were measured using an R.M. Young 05103 wind monitor (instrument intrinsic maximum measurement uncertainty of ± 0.3 m/s). All measurements were logged at 15 minute intervals. Data are available for download at www.mcmlter.org.

The continuous monitoring station was installed on the south side of the Garwood River in austral field season 2010–2011, ~ 8 m from the base of the ice cliff. The station was moved to the north side of the river at the end of the 2011–2012 field season due to deepening of the Garwood River channel.

Time lapse image data of the ice cliff were collected with a Canon a590IS digital camera installed atop the delta on the floor of Garwood Valley. Images of the entire ice cliff were acquired every 10 minutes from January 10, 2012 to January 28, 2012. Custom software written by the authors was used to synchronize time-lapse image data with data from the continuous monitoring station observed within the field of view of the camera. Images were matched with the nearest data logger measurement, such that each image is no more than 7.5 minutes before or after its corresponding data plot.

Thermal properties measurements were made using a Decagon Devices KD2 Pro thermal properties probe. Thermal conductivity, heat capacity, and thermal diffusivity were measured simultaneously.

1. Levy, J. S., Fountain, A. G., O'Connor, J. E., Welch, K. A. & Lyons, W. B. Garwood Valley, Antarctica: A new record of last glacial maximum to Holocene glaciofluvial processes in the McMurdo Dry Valleys. *Geological Society of America Bulletin* In Press (2013).
2. Denton, G. H. & Marchant, D. R. The geologic basis for a reconstruction of a grounded ice sheet in McMurdo Sound, Antarctica, at the last glacial maximum. *Geografiska Annaler: Series A, Physical Geography* **82**, 167–211 (2000).
3. Campbell, I. B. & Claridge, G. in *Proceedings of the Eighth International Conference on Permafrost* (Phillips, M., Springman, S. M. & Arenson, L. U.) 119–123 (Swets & Zeltinger, 2003).
4. Shaw, J. & Healy, T. R. The formation of the Labyrinth, Wright Valley, Antarctica. *New Zealand Journal of Geology and Geophysics* **20**, 933–947 (1977).
5. Bockheim, J. G. Permafrost distribution in the southern circumpolar region and its relation to the environment: a review and recommendations for further research. *Permafrost and Periglacial Processes* **6**, 27–45 (1995).
6. Swanger, K. M. & Marchant, D. R. Sensitivity of ice-cemented Antarctic soils to greenhouse-induced thawing: Are terrestrial archives at risk? *Earth and Planetary Science Letters* **259**, 347–359 (2007).
7. Schenk, T., Csatho, B. M., Ahn, Y., Yoon, T. & Shin, W. S. *DEM generation from the Antarctic LiDAR data: Site report.* (US Geological Survey, 2004).at <http://usarc.usgs.gov/lidar/lidar_pdfs/Site_reports_v5.pdf>.
8. Marchant, D. R. & Head, J. W. III. Antarctic dry valleys: Microclimate zonation, variable geomorphic processes, and implications for assessing climate change on Mars. *Icarus* **192**, 187–222 (2007).
9. Healy, T. R. Thermokarst—a mechanism of de-icing ice-cored moraines. *Boreas* **4**, 19–23 (1975).
10. Stuiver, M., Denton, G. H., Hughes, T. J. & Fastook, J. L. in *The Last Great Ice Sheets* (Denton, G. H. & Hughes, T. J.) 319–362 (Jogn Wiley and Sons, 1981).
11. Pollard, W., Doran, P. & Wharton, R. The nature and significance of massive ground ice in Ross Sea Drift, Garwood Valley, McMurdo Sound. *Royal Society of New Zealand Bulletin* **35**, 397–404 (2002).
12. Péwé, T. L. Multiple glaciation in the McMurdo Sound region, Antarctica: A progress report. *The Journal of Geology* 498–514 (1960).
13. Shindell, D. T. Southern Hemisphere climate response to ozone changes and greenhouse gas increases. *Geophysical Research Letters* **31**, L18209 (2004).
14. Arblaster, J. M. & Meehl, G. A. Contributions of external forcings to southern annular mode trends. *Journal of Climate* **19**, 2896–2905 (2006).
15. Chapman, W. L. & Walsh, J. E. A Synthesis of Antarctic Temperatures. *Journal of Climate* **20**, 4096–4117 (2007).
16. Lewkowicz, A. G. Headwall retreat of ground-ice slumps, Banks Island, Northwest Territories. *Canadian Journal of Earth Sciences* **24**, 1077–1085 (1987).
17. Lewkowicz, A. G. Rate of short-term ablation of exposed ground ice, Banks Island, Northwest Territories, Canada. *Journal of Glaciology* **32**, 511–519 (1986).
18. Burn, C. R. & Lewkowicz, A. G. Canadian Landform Examples-17 Retrogressive Thaw Slumps. *The Canadian Geographer* **34**, 273–276 (1990).
19. Lantuit, H. *et al.* Modern and Late Holocene Retrogressive Thaw Slump Activity on the Yukon Coastal Plain and Herschel Island, Yukon Territory, Canada. *Permafrost and Periglacial Processes* **23**, 39–51 (2012).
20. Lantuit, H. & Pollard, W. H. Fifty years of coastal erosion and retrogressive thaw slump activity on Herschel Island, southern Beaufort Sea, Yukon Territory, Canada. *Geomorphology* **95**, 84–102 (2008).
21. Lantuit, H. & Pollard, W. H. Temporal stereophotogrammetric analysis of retrogressive thaw slumps on Herschel Island, Yukon Territory. *Natural Hazards and Earth System Sciences* **5**, 413–423 (2005).
22. Niu, F., Luo, J., Lin, Z., Ma, W. & Lu, J. Development and thermal regime of a thaw slump in the Qinghai–Tibet plateau. *Cold Regions Science and Technology* **83–84**, 131–138 (2012).
23. Doran, P. T. *et al.* Antarctic climate cooling and terrestrial ecosystem response. *Nature* **415**, 517–520 (2002).
24. Sensitivity of Cenozoic Antarctic ice sheet variations to geothermal heat flux. **49**, 63–74 (2005).
25. Bromwich, D. H. *et al.* Central West Antarctica among the most rapidly warming regions on Earth. *Nature Geoscience* **6**, 139–145 (2012).
26. Nylen, T. H. Climatology of katabatic winds in the McMurdo dry valleys, southern Victoria Land, Antarctica. *Journal of Geophysical Research* **109**, D03114 (2004).
27. Hoffman, M. J., Fountain, A. G. & Liston, G. E. Surface energy balance and melt thresholds over 11 years at Taylor Glacier, Antarctica. *Journal of Geophysical Research* **113**, F04014 (2008).
28. Bliss, A. K., Cuffey, K. M. & Kavanaugh, J. L. Sublimation and surface energy budget of Taylor Glacier, Antarctica. *Journal of Glaciology* **57**, 684–696 (2011).
29. Fountain, A. G., Nylen, T. H., MacClune, K. L. & Dana, G. L. Glacier mass balances (19932001), Taylor Valley, McMurdo Dry Valleys, Antarctica. *Journal of Glaciology* **52**, 451–462 (2006).
30. Chinn, T. J. in *Physical and Biogeochemical Processes in Antarctic Lakes* **Antarctic Research Series Volume 59**, 1–51 (American Geophysical Union, 1993).
31. How important is terminus cliff melt?: a study of the Canada Glacier terminus, Taylor Valley, Antarctica. **22**, 105–115 (1999).
32. Hall, B. L., Denton, G. H., Fountain, A. G., Hendy, C. H. & Henderson, G. M. Antarctic lakes suggest millennial reorganizations of Southern Hemisphere atmospheric and oceanic circulation. *Proceedings of the National Academy of Sciences* **107**, 21355–21359 (2010).
33. Pufahl, D. E. & Morgenstern, N. R. The energetics of an ablating headscarp in permafrost. *Canadian Geotechnical Journal* **17**, 487–497 (1980).
34. Fountain, A. G., Pettersson, R. & Levy, J. S. A landscape on the threshold of change: The McMurdo Dry Valleys. in *Scientific Committee on Antarctic Research Open Science Conference* (2012).
35. Stanhill, G. & Cohen, S. Recent Changes in Solar Irradiance in Antarctica*. *Journal of Climate* **10**, 2078–2086 (1997).
36. Campbell, G. S. *An introduction to environmental biophysics.* 14–19 (Springer-Verlag, 1977).
37. Benn, D. I. *et al.* Response of debris-covered glaciers in the Mount Everest region to recent warming, and implications for outburst flood hazards. *Earth-Science Reviews* **114**, 156–174 (2012).
38. Corsini, A. *et al.* Estimating mass-wasting processes in active earth slides–earth flows with time-series of High-Resolution DEMs from photogrammetry and airborne LiDAR. *Natural Hazards and Earth System Sciences* **9**, 433–439 (2009).
39. Schiefer, E. & Gilbert, R. Reconstructing morphometric change in a proglacial landscape using historical aerial photography and automated DEM generation. *Geomorphology* **88**, 167–178 (2007).
40. Daehne, A. & Corsini, A. Kinematics of active earthflows revealed by digital image correlation and DEM subtraction techniques applied to multi-temporal LiDAR data. *Earth Surf. Process. Landforms* **38**, 640–654 (2012).
41. Dewitte, O. & Demoulin, A. Morphometry and kinematics of landslides inferred from precise DTMs in West Belgium. *Natural Hazards and Earth System Science* **5**, 259–265 (2005).
42. Lorenz, D. The Effect of the Long-wave Reflectivity of Natural Surfaces on Surface Temperature Measurements Using Radiometers. *Journal of Applied Meteorology* **5**, 421–430 (1966).

Acknowledgements

This work was supported by the U.S. National Science Foundation (NSF) Antarctic Earth Sciences program under award ANT-1343835 to Levy, Fountain, and W. B. Lyons. Many thanks go to the extensive team that made this research possible, notably, to Dustin Black

for bringing the Garwood Valley ice cliff to the attention of the research team, and to all the PHI pilots and ground staff for providing reliable and safe access to the site; to Thomas Nylen, Hasan Basagic, Rickard Pettersson, and James Jerome Bethune for field assistance; to Deb Leslie for stable isotope analyses of ice samples; to the Arizona Accelerator Mass Spectrometry (AMS) Laboratory for radiocarbon dating services; and to Paul Morin and the Polar Geospatial Center for access to satellite image data. Airborne light detection and ranging (LiDAR) topography used in this paper was kindly made possible through a joint effort from the NSF, the National Aeronautics and Space Administration, and the U.S. Geological survey, with basic post-processing from the Byrd Polar Research Center. Ground based LiDAR was collected by UNAVCO. This manuscript has benefited from thoughtful reviews from two anonymous reviewers.

Author contributions

J.L. conducted fieldwork, LiDAR and continuous station data analysis, and contributed text for the manuscript. A.F. conducted the static station monitoring experiment and contributed manuscript text. J.D. and J.H. provided the time lapse data analysis and contributed manuscript text. M.O. contributed the LiDAR data collection and analysis and contributed manuscript text. D.M. contributed text to the manuscript. J.W. conducted time lapse data analysis and contributed figures to the supplementary material. All authors reviewed the manuscript.

Additional information

Supplementary information accompanies this paper at http://www.nature.com/scientificreports

Competing financial interests: The authors declare no competing financial interests.

How to cite this article: Levy, J.S. *et al*. Accelerated thermokarst formation in the McMurdo Dry Valleys, Antarctica. *Sci. Rep.* **3**, 2269; DOI:10.1038/srep02269 (2013).